RSC Advances

PAPER

View Article Online
View Journal | View Issue

Cite this: *RSC Adv.*, 2022, **12**, 35639

Cd-doped $Ag_2O/BiVO_4$ visible light Z-scheme photocatalyst for efficient ciprofloxacin degradation†

Arup Kumar De, Uttam Kumar, Neha Jatav and Indrajit Sinha *

Received 13th November 2022
Accepted 6th December 2022

DOI: 10.1039/d2ra07200a

rsc.li/rsc-advances

Foreign element doping can produce new photocatalysts with different band edge positions and adsorption properties. A composite of such a doped semiconductor with another component should enhance its photocatalytic properties towards a target substrate. The present investigation used a simple hydrothermal protocol to prepare Cd-doped Ag_2O nanoparticles. The Cd-doping of Ag_2O nanoparticles changed its valence band maximum position from 0.8 eV (for undoped Ag_2O nanoparticles) to 2.67 eV with a slight narrowing of the Ag_2O bandgap. A combination of DFT calculation and XRD results showed that the dopant Cd substituted Ag in the Ag_2O lattice. The doped material is an effective photocatalyst for ciprofloxacin degradation but with poor recyclability. The joining of a $BiVO_4$ part to the Cd-doped Ag_2O nanostructures gave a composite with improved photocatalytic activity and recyclability towards ciprofloxacin degradation. DFT calculations showed that $BiVO_4$ has a higher oxygen affinity than Cd-doped Ag_2O. The XPS characterization of the composite and appropriate active species scavenger experiments demonstrated a Z-scheme mechanism. Superoxide radicals play a critical role in CIP degradation.

1. Introduction

Doping a semiconductor photocatalyst can change its electronic structure and induce charge separation, resulting in delayed recombination.[1–5] The bandgap, valence band (VB), or conduction band (CB) positions are also affected. For instance, Natu *et al.* reported Co doping shifts the VB position of NiO.[6] In another study, Wang *et al.* executed a detailed DFT investigation of the effect of oxygen doping on the Ta_3N_5 photocatalyst. The oxygen doping changed the bandgap and band edges of the Ta_3N_5 photocatalyst.[7] Doping also affects the adsorption properties of the parent photocatalyst.[8–10] Hence, doping affects the photocatalyst bandgap, band positions, and adsorption behavior. It effectively produces a new photocatalyst with different photocatalytic properties.

More intensive use of medium and small bandgap (corresponding to the visible range) semiconductors is necessary for fabricating photocatalysts that can optimally utilize the visible part of the solar spectrum. For instance, photostability or photo corrosion of (small bandgap) Ag_2O has hampered its photocatalytic applications. Doping Ag_2O and its composite formation with another semiconductor can significantly reduce the problem while improving excited species charge separation.[11] A recent study on Zn-doping in Ag_2O revealed that such inclusion could shift the VB of the Ag_2O to a higher positive value.[12] In another report, Sr doping also resulted in Ag_2O bandgap widening.[13] Recently, De *et al.* showed that Ni doping could shift the VB and CB edge of the Ag_2O photocatalyst to a more positive and less negative value. The higher valence Ni^{2+} substituted Ag^+ to give the host system excess electrons.[14] Thus, doping Ag_2O can provide a photocatalyst with a tunable band structure with distinct properties.

Despite the advantages of doped photocatalysts, the band gap still restricts their VB and CB positions. A composite of two semiconducting components with staggered band gaps (band alignment) can further improve charge separation. Two individual semiconductors joined together can act as two half-cells for oxidation and reduction purposes.[15,16] Photoexcitation can concentrate electrons in the less positive CB component and holes in the part with the more positive VB.[28] The latter is called a Z-scheme photocatalyst. It has improved reduction and oxidation driving forces. Thus, Z-scheme photocatalysts can cover target a more comprehensive range of redox reactions. A Z-scheme mechanism can take place when both semiconductor components of the composite photocatalyst are either n- or p-type. Combining a doped semiconductor with another can change the photocatalyst reduction and oxidation driving forces along with the excited species charge separation.[17–21] Hence, a doped Ag_2O material as a part of a composite should give an improved photocatalyst. There have been a few investigations on Ag_2O-based composites (or photocatalytic heterostructures).

Department of Chemistry, Indian Institute of Technology (Banaras Hindu University), Varanasi 221005, India. E-mail: isinha.apc@iitbhu.ac.in

† Electronic supplementary information (ESI) available. See DOI: https://doi.org/10.1039/d2ra07200a

For instance, there are reports on the fabrication and evaluation of ZnO/Ag/Ag_2O, Ag_2O/TiO_2, $BiVO_4$/Ag/Ag_2O, Ag_2O/Bi_2O_3, *etc.*, photocatalysts.[22–25] But to date, we have not encountered any doped Ag_2O-based composite photocatalyst study in the literature.

In the present research, we investigated the photocatalytic properties of Cd-doped Ag_2O and its composite with $BiVO_4$. Note there is no report in the literature on either the synthesis or the photocatalytic properties of Cd doped-Ag_2O nanoparticles. The first part of this research evaluated whether Cd substitutes Ag or occupies an interstitial position through density functional theory (DFT) calculation of the formation energies of the two models. Simultaneously, Cd-doped Ag_2O nanoparticles were prepared by a hydrothermal precipitation protocol. X-ray diffraction (XRD) results agreed with the DFT defect formation energy prediction. X-ray photoelectron spectroscopy (XPS) investigated the chemical species and the VB position in the Cd-doped Ag_2O nanoparticles. Separately, a well-established hydrothermal protocol was employed to prepare monoclinic $BiVO_4$. In the next step, another hydrothermal strategy joined these nanoparticles to Cd-doped Ag_2O nanostructures. The prepared composite particles were characterized using different techniques. The composite nanoparticles were evaluated for photocatalytic ciprofloxacin (CIP) degradation activity under visible light irradiation.

CIP is frequently administered to human patients and excreted in a partially metabolized state. The latter makes the target microorganisms in the environment resistant to the antibiotic.[26,27] Photocatalytic activities with different active species scavenger molecules probed the underlying photocatalysis mechanism. Parallelly, DFT calculations ascertained the adsorption energies of oxygen and H_2O on the Cd-doped Ag_2O and $BiVO_4$ surfaces. The adsorption information along with detailed photocatalysis experimental data helped us to propose a plausible photocatalysis mechanism.

2. Experimental and computational methods

2.1. Sample preparation

2.1.1. Synthesis of Cd doped Ag_2O. A hydrothermal protocol was followed to prepare Cd-doped Ag_2O. Two millimoles (mmol) of $AgNO_3$ (Merck) were fully dissolved in 50 ml deionized double distilled water (DDDW) with continuous stirring on a magnetic stirrer. Then, 0.2 M NaOH was added drop-by-drop into the stirring solution until the solution pH reached 11. A brown-colored precipitate was formed during the addition. The stirring was continued for 15 minutes. Next, the desired amount of $Cd(NO_3)_2 \cdot 4H_2O$ (Merck) aqueous solution was added to the previously obtained mixture. Stirring was continued for another 15 minutes, and then the reaction mixture was transferred to a 100 ml stainless steel autoclave. The latter was treated in a hot air oven at 180 °C for 24 hours. We prepared three different compositions of Cd-doped Ag_2O samples abbreviated as D1, D2, and D3. The precursor salts for preparing these samples contained 0.3, 0.62, and 1.25 mole percent of $Cd(NO_3)_2 \cdot 4H_2O$. $AgNO_3$ made up the rest of the salt precursor composition. In addition, the pure Ag_2O (denoted as D0) was also synthesized by the same hydrothermal protocol but without $Cd(NO_3)_2 \cdot 4H_2O$ addition.

2.1.2. Synthesis of $BiVO_4$. Aqueous solutions of $Bi(NO_3)_3 \cdot 5H_2O$ (Merck) and NH_4VO_3 (HIMEDIA) were prepared in two separate beakers. In one beaker (A), 20 ml of 4 M HNO_3 was directly mixed with four mmol of $Bi(NO_3)_3 \cdot 5H_2O$ salt with continuous stirring until the formation of a clear solution. In another beaker (B), four mmol of NH_4VO_3 was dissolved in 20 ml of 4 M NaOH by continuous stirring. Stirring was continued in both beakers for 30 minutes. The solution in beaker B was added drop-by-drop into beaker A in the next step. The formation of a yellow-colored precipitate was observed. Next, the reaction mixture pH was adjusted to 7 by adding an appropriate amount of NaOH. This reaction mixture was stirred for another 25 minutes and then transferred to a 100 ml autoclave reactor for hydrothermal treatment at 180 °C. After 20 hours of hydrothermal treatment, the reaction mixture was allowed to cool. The precipitate formed was separated and washed with DDDW several times until the water used in washing had neutral pH. Finally, the as-prepared precipitate was washed with ethanol and dried at 60 °C under a hot air oven to get the $BiVO_4$ nanoparticles (abbreviated by 'V0' in the rest of the paper).

2.1.3. Synthesis of $BiVO_4$/Cd-doped Ag_2O. The D1 sample (of Cd-doped Ag_2O) was mixed with 5, 10, and 20% weight percent of $BiVO_4$ nanoparticles in 60 ml DDDW to prepare three separate systems abbreviated as D1/5V, D1/10V, and D1/20V, respectively. The three mixtures were stirred for 4 hours to induce interaction between Cd-doped Ag_2O and $BiVO_4$ nanoparticles. These mixtures were transferred to 100 ml autoclave reactors and subjected to hydrothermal treatment for twelve hours at 120 °C. Afterward, the prepared material was separated from the supernatant and dried at 50 °C overnight in a hot air oven.

2.2. Characterization

All samples' powder XRD data were recorded on a Rigaku Miniflex 600 (RIGAKU Corporation) instrument. The instrument utilized a Cu Kα irradiation source (λ = 1.54056 Å) at a scan rate of 5° min^{-1} and step size of 0.02 during the data collection. The applied current was 15 mA, and the accelerating voltage was 40 kV. Transmission electron microscopy (TEM) images were recorded on Tecnai G2 20 TWIN (EDAX Inc.) instrument using 200 kV accelerating voltage. The X-ray photoelectron spectra (XPS) were recorded on a K-alpha Thermo Fisher Scientific XPS instrument. Agilent Cary 60 UV-vis spectrophotometer measured the UV-visible absorption spectra of all liquid samples. The UV-vis reflectance spectra of all the solid samples were collected on the Shimadzu UV-2600 spectrophotometer. Electrochemical analysis was performed on the Metrohm Multi auto lab/M204 instrument.

2.3. Computational methods

The plane-wave density functional theory (DFT) calculations were done on the MedeA VASP (Vienna *ab initio* simulation

package) software. The calculations used generalized gradient approximation Perdew–Burke–Ernzerhoff (GGA-PBE) exchange–correlation functional and the projected wave (PAW) pseudo-potentials. A 2 × 2 × 2 supercell was built from the Ag_2O unit cell (ICDS Card No. 4318188) and was optimized using 2 × 2 × 2 *k*-points and 520 eV energy cut-off. The optimized supercell is labeled as P0 in the rest of the manuscript. The doped Cd atom could substitute an Ag atom or occupy an interstitial position in the Ag_2O lattice. Thus, in one model (denoted as P1), one Cd substituted an Ag atom in the Ag_2O supercell. In another model (denoted as P2), a Cd atom was placed in an interstitial position of the Ag_2O lattice. These two models were optimized with the same calculation parameters as mentioned above. After that, the defect formation energies of the two doped systems were calculated using the following equations.

$$E_f(\text{sub}) = E_{\text{defect}}(\text{P1}) - [E_{\text{perfect}}(\text{P0}) - \mu_{\text{Ag}} + \mu_{\text{Cd}}] \quad (1)$$

$$E_f(\text{inter}) = E_{\text{defect}}(\text{P2}) - [E_{\text{perfect}}(\text{P0}) + \mu_{\text{Cd}}] \quad (2)$$

Here, E_f(sub) and E_f(inter) are the defect formation energy of the substituted and interstitially doped systems. E_{defect}(P1), E_{defect}(P2), and E_{perfect}(P0) are the energies of the P1, P2, and P0 models, respectively. The energy per atom in Ag (unit cell is referred from Crystallography Open Database (COD) 9011607) and Cd (COD 9012436) unit cells gives the chemical potentials of the Ag and Cd (μ_{Ag} and μ_{Cd}).

The adsorption energies (E_{abs}) of H_2O and O_2 on Cd-doped Ag_2O(200) and $BiVO_4$(112) surfaces were evaluated by slab model calculations using eqn (3). First, the Ag_2O supercell was cleaved to obtain its (200) surface, and then an Ag atom was replaced with a Cd atom to construct the Cd-doped Ag_2O(200) slab. Similarly, the $BiVO_4$ supercell was cleaved to get its (112) surface. A four-layer slab with a vacuum of 10 Å was considered for the Cd-doped Ag_2O(200) slab and the $BiVO_4$(112) surface models. The dimensions for Cd doped Ag_2O(200) and $BiVO_4$(112) slabs were 6.69 Å × 6.69 Å × 28.92 Å and 6.93 Å × 7.32 Å × 96.99 Å.

$$E_{\text{abs}} = E_{\text{slab+adsorbate}} - (E_{\text{slab}} + E_{\text{adsorbate}}) \quad (3)$$

Here, $E_{\text{slab+adsorbate}}$ is the energy of the slab after interaction with the adsorbate molecule. E_{slab} and $E_{\text{adsorbate}}$ are the energies of the individual free slab and the free adsorbate molecule.

2.4. Photocatalysis experiment details

A 2 ml aqueous solution of CIP (10 ppm) at pH ∼ 3 and 100 μl of the re-dispersed photocatalyst aqueous suspension (1 mg ml^{-1}) were mixed properly in a 4 ml quartz cuvette. The mixture was allowed to stand in a dark environment for 35 minutes under continuous stirring until adsorption–desorption equilibrium. Then the cuvette was kept under visible light irradiation (14 W Philips LED bulb with an intensity of 720 W m^{-2}). The absorbance of the reaction mixture was recorded at regular time intervals to monitor the photocatalytic activities of the synthesized materials. Turnover frequencies (TOF) were also calculated.

2.5. Electrochemical measurements

First, the re-dispersed photocatalyst suspension was cast on the working electrode. The Ag/AgCl (reference electrode), Pt (counter electrode), and glassy carbon (working electrode) electrodes were assembled in 0.5 M Na_2SO_4 solution to measure electrochemical impedance. The impedance data were collected between −0.9 V to +0.9 V potential (at a fixed 0.005 V amplitude and ∼1 kHz frequency). Mott–Schottky plots and the CB position of the D1 photocatalyst were generated from the potential *vs.* NHE (normal hydrogen electrode) data graph. The latter was converted from the potential (in volts 'V') *vs.* Ag/AgCl electrode using the following relation,[28,29]

$$V\,(\text{NHE}) = V\,(\text{Ag/AgCl}) + 0.059\text{pH} + 0.197 \text{ (here pH} = 7)$$

3. Results and discussion

3.1. Structural properties

Fig. 1a displays the powder XRD pattern of the undoped (D0) and different Cd-doped Ag_2O nanoparticle samples (D1 and D2). All the peaks in the XRD plots of D0 and D1 match the standard face-centered cubic (FCC) Ag_2O (JCPDS Card No. 75-1532) pattern. Other phases are not present in the D1 sample. Nonetheless, the XRD of D2, in addition to the FCC Ag_2O peaks, also displays three small peaks of the FCC Ag phase. The formation of reduced Ag is due to the excess electrons supplied by the dopant when added beyond a specific limit. Furthermore, the XRD pattern of sample D3 displayed peaks of phases other than FCC Ag_2O and Ag (Fig. S1 in ESI†) when the dopant level increased to 1.25 mol%.

Fig. 1b compares the (111) plane peak positions of D0, D1, and D2 samples. The (111) peak position shifts towards higher 2θ regions in doped samples, indicating lattice contraction. Nevertheless, the peak shift is not uniform. The smallest dopant percentage sample (D1) gave the maximum peak shift. The Cd^{2+} and Ag^{+} have effective ionic radii of 95 and 115 pm. As mentioned earlier, the dopant (Cd^{2+}) has two choices: it can substitute one Ag or go into the interstitial sites in the Ag_2O lattice. Lattice contraction is only possible if the smaller Cd substitutes Ag in the Ag_2O lattice. Thus, the XRD pattern of the D1 sample shows that Cd substitutes Ag in the Ag_2O lattice without FCC Ag formation.

Fig. 2 compares the powder XRD patterns of the composite materials with those of $BiVO_4$ (BV) and D1 samples. The XRD pattern of sample V0 matches the standard body-centered monoclinic (JCPDS Card No. 831699) phase of $BiVO_4$. The major peaks in the XRD at 18.9°, 29°, 30.7°, 42.5°, and 53.4° are indexed to the (011), (112), (004), (015), and (116) planes of the body-centered monoclinic $BiVO_4$. The XRD of all composite samples showed the presence of both Ag_2O and $BiVO_4$ phases, indicating nanocomposite formation.[30] Hereafter, the investigation concentrates on D1/10V sample characterization because of its enhanced photocatalytic activity (compared to D1/5V and D1/20V composites) towards CIP. Fig. 3a and b exhibit the TEM and high-resolution TEM (HRTEM) images of the D1/10V

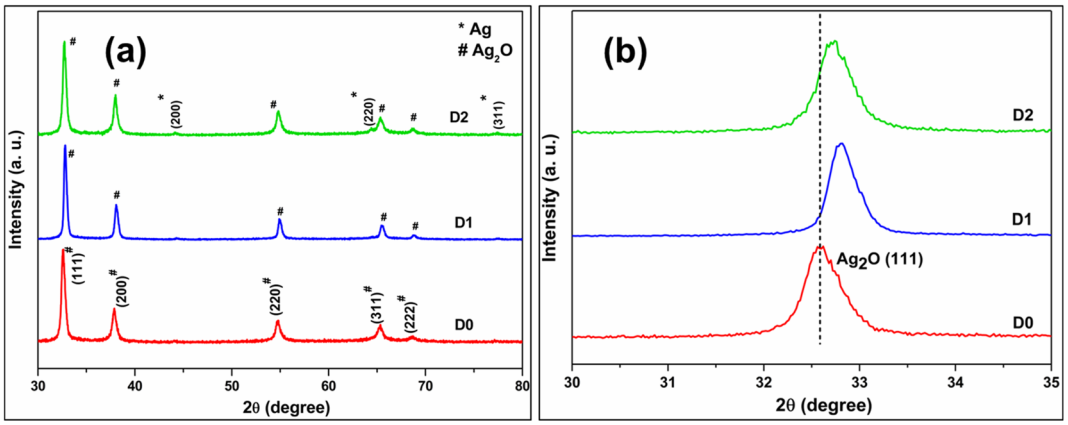

Fig. 1 (a) The powder XRD pattern of undoped (D0) and doped samples (D1 and D2) (b) zoom-in Ag_2O(111) peak part.

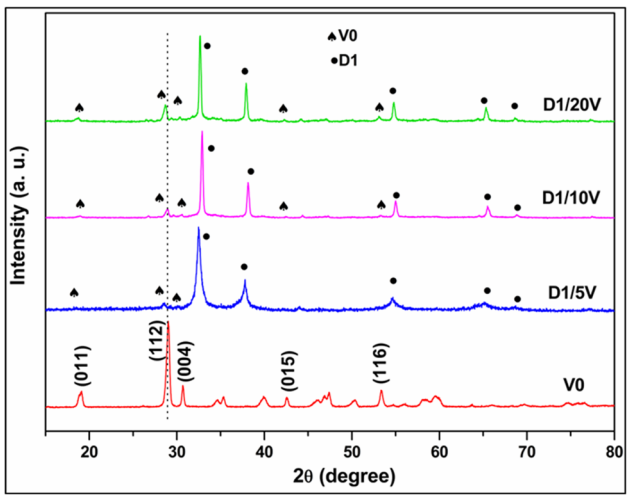

Fig. 2 Comparison of powder XRD patterns of $BiVO_4$ nanoparticles and composite samples (D1/5V, D1/10V, D1/20V).

composites. The high-resolution image of the encircled region (in Fig. 3a) shows two types of fringes adjacent to each other. These fringe spacings match the *d*-spacing of $BiVO_4$(011) and Ag_2O(111) planes, confirming D1/10V composite formation. Elemental mapping supports the presence of all the constituent elements of the D1/10V sample (Fig. S2 in the ESI†).

3.2. XPS analysis

XPS investigation gives information about elements and their oxidation states in a material. Fig. S3 (ESI†) shows the Ag 3d high-resolution XPS plots of samples D0 and D1. The Ag $3d_{3/2}$ and Ag $3d_{5/2}$ peaks at 374.28 and 368.26 eV for D0 shift to 373.75 and 367.73 eV for the D1 sample. The extra electrons injected into the system by the Cd dopant made D1 electron-rich, causing the shift of respective Ag 3d peaks to lower binding energies. The XPS survey spectrum of the D1/10V composite shows the presence of Ag, Bi, V, and O elements in the composite (see Fig. S4 in the ESI†). Fig. 4a compares the Ag 3d region high-resolution XPS plots of D1 and D1/10V samples. The Ag $3d_{5/2}$ and Ag $3d_{3/2}$ peaks at 367.71 and 373.74 eV for D1 shifted to higher values (Ag $3d_{5/2}$ at 368.15 and Ag $3d_{3/2}$ at 374.18 eV) in the D1/BV10 composite spectrum. Simultaneously, the Bi 4f spectrum with two peaks corresponding to Bi $4f_{7/2}$ at 158.96 and Bi $4f_{5/2}$ at 164.26 eV shifted to lower binding energy in the composite sample (Bi $4f_{7/2}$ at 158.70 and Bi $4f_{5/2}$ at 164.01 eV) (Fig. 4b). A similar shift to lower binding energy was also observed for the vanadium 2p peaks (see Fig. S5 in the ESI†). The shift to higher binding energies of Ag 3d peaks and lower binding energies of the Bi 4f peaks implies electron transfer from the Cd doped Ag_2O (D1) to $BiVO_4$ (V0). Fig. 4c and d display the valence band XPS plots of D1 and D1/10V samples. The VB edge of the D1 sample is at 2.67 eV, and $BiVO_4$ (V0) is at 1.34 eV. Note that the VB position of the D0 (undoped Ag_2O) sample is at 0.8 eV (see Fig. S6 in the ESI†). Hence, Cd-doping of Ag_2O causes a severe shift in the VB (E_{VB}) position of the sample. A Z-scheme electron transfer mechanism seems to operate in this composite since the component with more negative CB ($BiVO_4$) becomes electron-rich, while the Cd-doped Ag_2O part becomes electron-deficient.

3.3. The bandgap

The bandgap of a photocatalyst is essential to propose a reasonable photocatalytic mechanism. The bandgap is the energy difference between VB and CB edge. The Tauc plot is derived from the solid-state UV-visible absorption data using eqn (4).

$$(\alpha h\nu)^{1/n} = (h\nu - E_g) \quad (4)$$

Here, α is the molar absorption coefficient, h is Planck's constant, ν is the frequency of the incident light and n denotes the transition exponent. The value of n is $\frac{1}{2}$ for direct and 2 for indirect transition, respectively. The x-axis intercept of the fit to the linear part of the Tauc plot gives the bandgap (E_g) of the tested material. Fig. 5a represents UV-visible absorption data of the D1 and V0 samples in solid powder form. The Tauc plots of D1 and V0 samples show direct bandgaps of 1.47 and 2.52 eV, respectively (see Fig. 5b and c). Combining the E_{VB} values (see the valence band XPS spectra of D1 and V0 samples in Fig. 4c

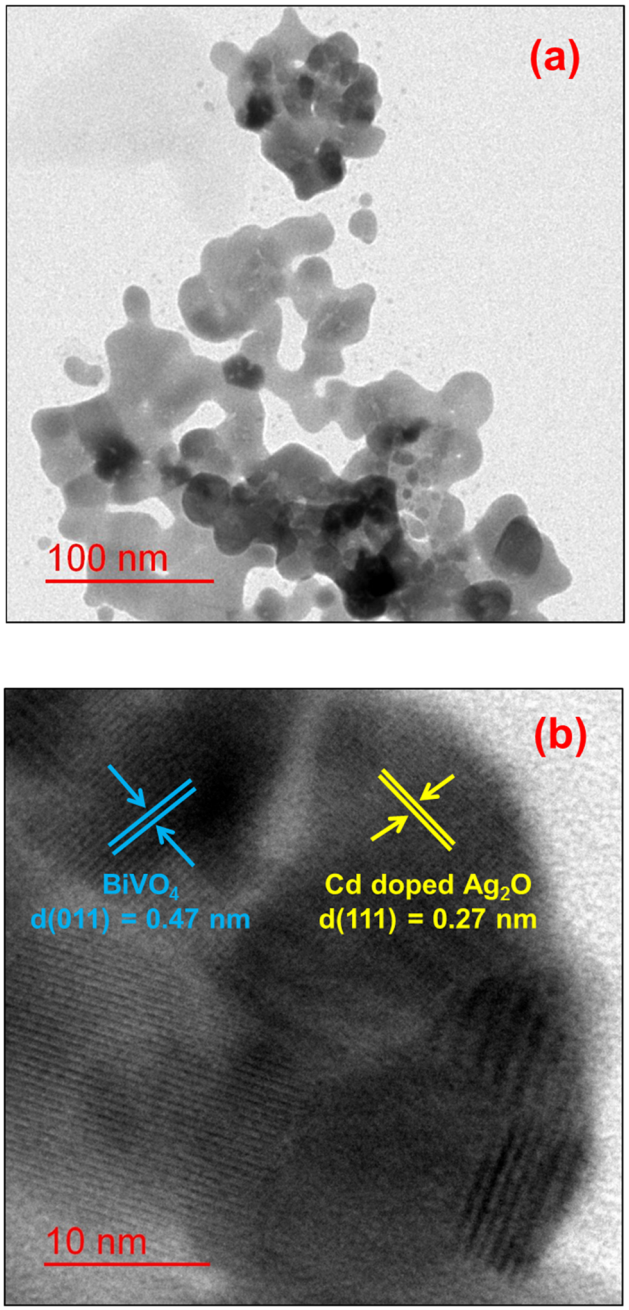

Fig. 3 (a) TEM and (b) HRTEM images of the D1/10V sample.

and d respectively) and the band gaps (from the Tauc plot) of D1 and V0 samples give us their relative E_{CB} (or CB) positions. Since bandgap is the energy difference between VB and CB edge, the formula $E_{CB} = E_{VB} + E_g$ gives the CB of D1 at 1.2 eV, and that of V0 at −1.18 eV.

3.4. Electrochemical studies

Electrochemical impedance spectroscopy (EIS) measurements are associated with the charge carriers' recombination kinetics. A lower semicircle diameter of the Nyquist plot indicates lower resistance and greater charge separation. Fig. S7a (ESI†) displays the Nyquist plots for the D1, V0, and D1/10V photocatalyst samples. The D1/10V composites showed lower semicircle diameter, indicating a better charge separation than its components. Fig. S7b (ESI†) gives the Mott–Schottky plot of the D1 catalyst. The positive slope of the plot gave proof of n-type conductivity in the D1 material.

3.5. DFT results

The DFT calculation supports the experimental results and helps to develop a plausible mechanism during the photocatalytic reaction. The formation energy was calculated using eqn (1) and (2) in Section 2.3. The formation energies of P1 (substitutional) and P2 (interstitial) models are −0.43 and 0.53 eV, respectively. Thus, substitutional doping is more favorable than interstitial doping, in agreement with the XRD result.

Table 1 tabulates the adsorption energies of H_2O and O_2 adsorption on Cd-doped Ag_2O and $BiVO_4$ surfaces. It also gives distances between different atoms in the adsorbate molecule and those on the adsorbent surface. The adsorption energies show that H_2O adsorption on the Cd-doped Ag_2O surface is more favorable than $BiVO_4$. Similarly, O_2 adsorption on the $BiVO_4$ surface gave more negative energy than on the Cd-doped Ag_2O surface. Fig. S8a and b (in the ESI†) show adsorption of H_2O on Cd-doped $Ag_2O(200)$ surface and O_2 molecule on $BiVO_4(112)$ surface. The H_2O molecule adsorbed on the Cd-doped Ag_2O surface *via* interaction (distance = 1.79 Å) between H(2) (in H_2O) and O(4) (in Cd-doped Ag_2O surface). Upon the interaction with the Cd-doped Ag_2O surface, one of the O–H bonds in the H_2O molecule got elongated from 0.97 to 1.00 Å (in Table 1), indicating H_2O activation on the Cd-doped Ag_2O surface. Similarly, the O_2 molecule interacted with vanadium (shown by the dotted line in Fig. S8b†) on the $BiVO_4$ surface. The O_2 bond elongated from 1.24 to 1.46 Å (in Table 1), showing O_2 activation on the $BiVO_4$ surface.

3.6. Photocatalytic properties

The photocatalytic activity of the synthesized materials was evaluated for visible light photodegradation of CIP. Fig. 6a compares the photocatalytic activities of different samples toward CIP photodegradation. The D1/10V composite exhibits the maximum photocatalytic activity. It is also reflected in the synthesized photocatalysts' (D1, V0, D1/5V, D1/10V, and D1/20V) turnover frequency (TOF) and rate constant values (see Table S1 in the ESI†). Efficient light absorption by a composite photocatalyst's components is a factor critical to its photocatalytic performance. Here, 10 mol% loading of $BiVO_4$ on Cd-doped Ag_2O (D1) is optimum for efficient light absorption. Increasing this percentage blocked the light absorption of the doped Ag_2O surface and decreased the photocatalytic performance. Thus, the TOF of D1/10V is the maximum. Fig. 6b shows that the CIP degradation results on D1, V0, and their composites follow pseudo-first-order reaction kinetics. The following equation expresses the first-order reaction kinetics,

$$-\ln(C/C_0) = k_{app}t \quad (5)$$

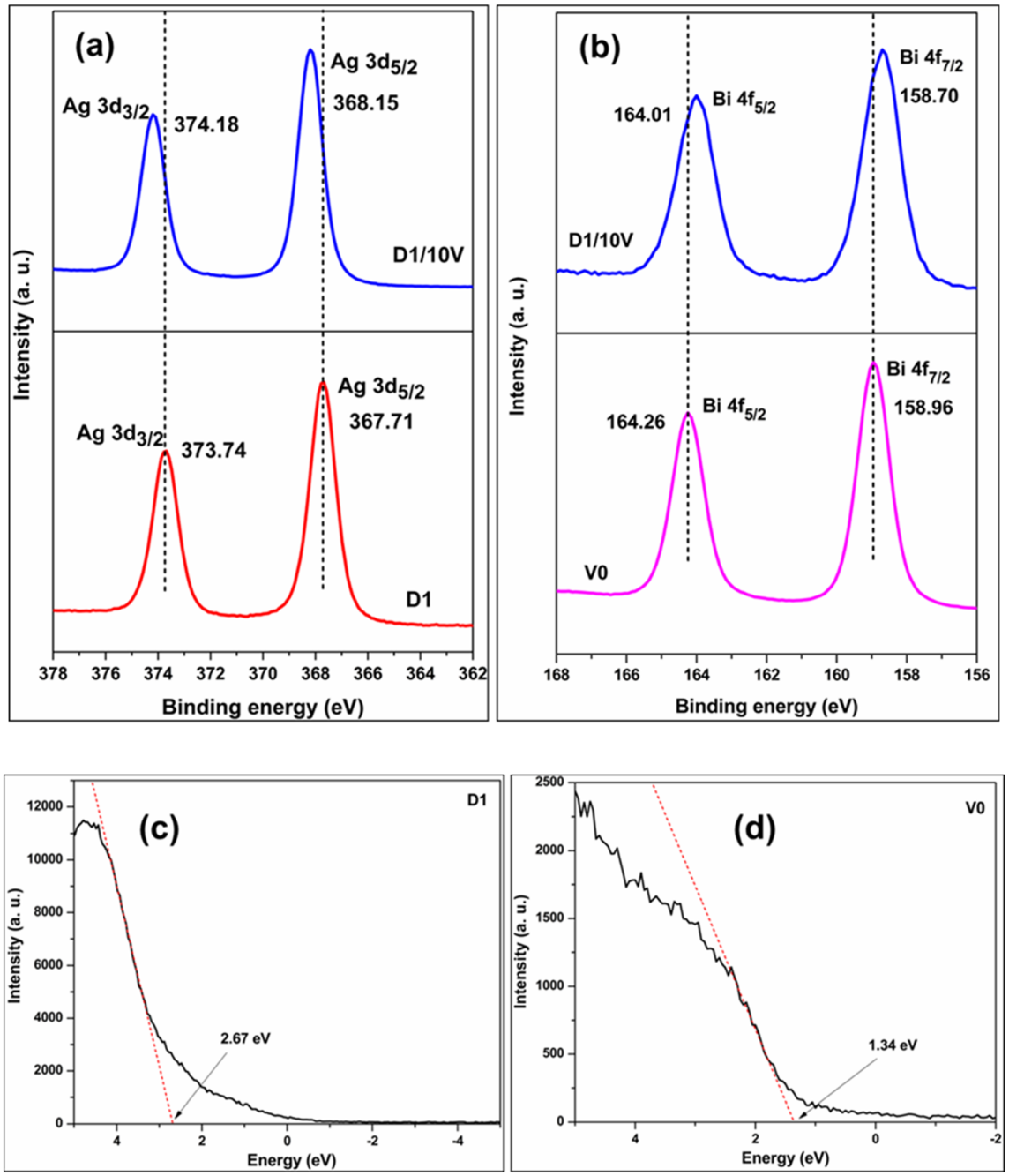

Fig. 4 (a) Ag 3d comparison of D1 and D1/B10 (b) Bi 4f comparison of V and D1/10V. The valence band XPS of (c) D1 and (d) V0.

Here, C_0 is the initial CIP concentration in the aqueous medium, C denotes the CIP concentration at time t, k_{app} is the apparent rate constant, and t is photocatalysis reaction time. Photocatalysis experiments were performed with scavengers like isopropyl alcohol (IPA) for hydroxyl radicals, KI for holes, and *p*-benzoquinone (PBQ) molecules for superoxide radicals. Fig. 6c displays the results of the scavenging experiments on the photocatalyst D1/10V. The presence of IPA gives higher catalytic activity compared to without scavenger. The IPA can also act as an electron donor and increase charge separation during photocatalysis.

On the contrary, the photocatalytic activity is drastically reduced in the presence of KI and PBQ scavengers. It indicates that both holes and superoxides contribute to photocatalytic CIP degradation. Fig. 6d shows reusability results during the photocatalysis of the D1/10V sample. This photocatalyst shows high recyclability compared to the D1 catalyst. Thus, D1 alone is not a good photocatalyst for CIP degradation. But it is an

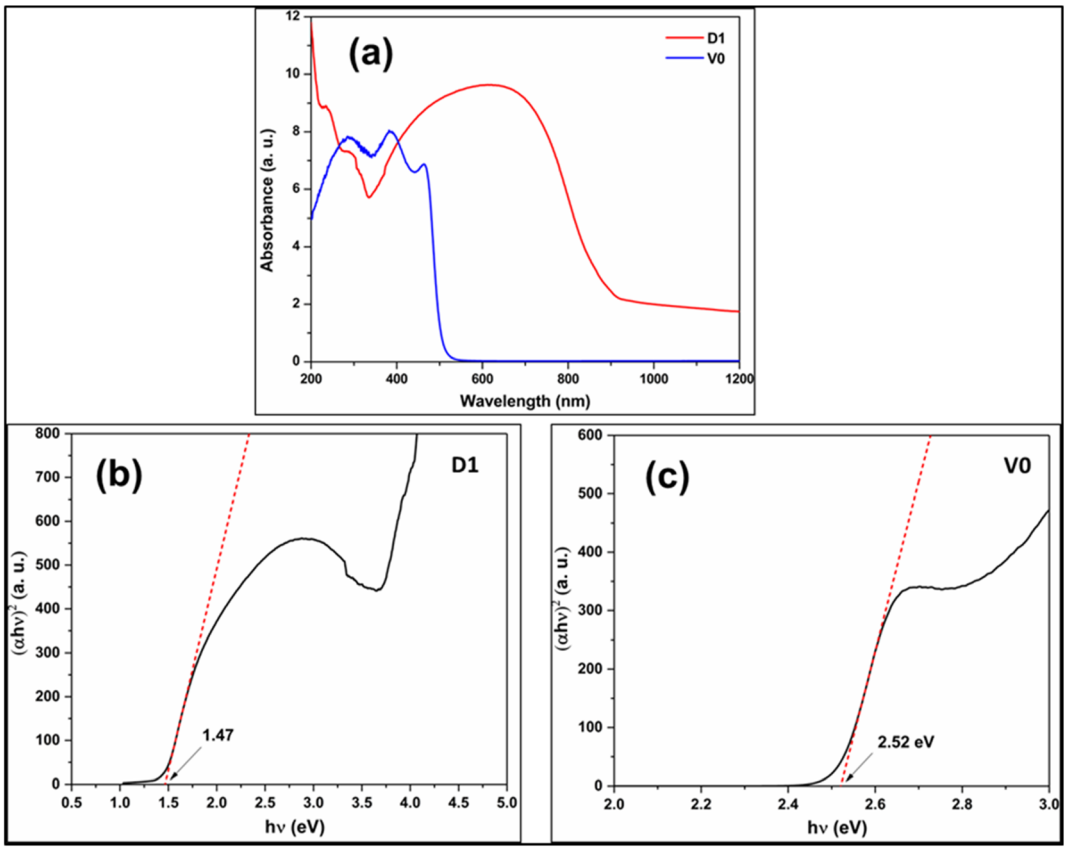

Fig. 5 (a) The UV-visible absorption spectrum of D1 and V0 samples. The Kubelka munk Tauc plot of (b) D1 and (c) V0.

efficient photocatalyst for CIP degradation as a composite with $BiVO_4$. The composite photocatalyst D1/10V exhibited a TOF value comparable with other composites reported (earlier) in the literature (see Table 2).

Two additional control photocatalytic experiments were performed by replacing water with acetonitrile (MeCN) as the solvent. The first experiment was done without oxygen purging. No CIP degradation (as shown in Fig. 7a) was observed under these circumstances. The second control experiment checked CIP degradation in MeCN medium and O_2 purging. In contrast to the first experiment, this time, there was little CIP degradation (see Fig. 7b). It indirectly proved CIP is oxidized with the help of externally purged O_2. The first control experiment shows that CIP degradation does not occur without water. Earlier scavenger experiments have already shown that superoxides are the dominant active species in CIP degradation. Superoxide radicals can be generated only by reducing oxygen molecules. The latter's sustained source can only be water oxidation (in the absence of any other substance in the reaction mixture). Thus, these two MeCN control experiments show that water oxidation plays a role in CIP degradation, and CIP cannot be photocatalytically degraded without water.[35]

3.7. Plausible mechanism

Fig. 8 displays a schematic diagram for the photocatalytic mechanism of CIP degradation. The VB and CB edge positions of Cd-doped Ag_2O and $BiVO_4$ were derived from results presented in Sections 3.2 and 3.3. Under visible light irradiation,

Table 1 Adsorption energies and interatomic distances for adsorption of H_2O and O_2 on considered Cd-doped Ag_2O and $BiVO_4$ surfaces

	E_{ads} (eV)		Distance (Å)		
Slab surface	H_2O	O_2		Before adsorption	After adsorption
Cd doped Ag_2O(200)	−1.56	−1.68	H1–O9	0.97	0.97
			H2–O9	0.97	1.00
			H2–O4	1.75	1.79
$BiVO_4$(112)	−0.27	−4.39	O33–O34	1.24	1.46
			V3–O33	1.82	2.02
			V6–O34	1.81	1.90

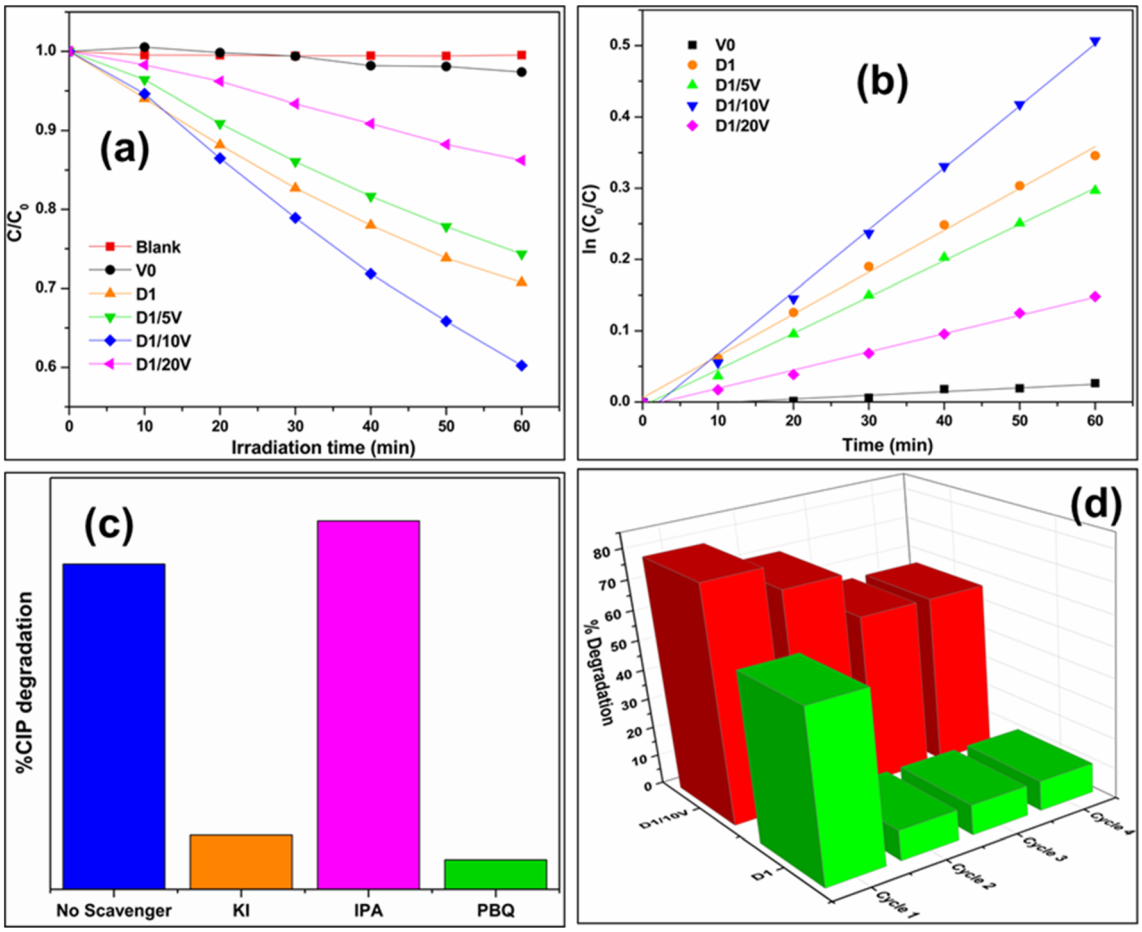

Fig. 6 (a) Comparison of CIP photodegradation for composites samples with component catalyst (b) kinetics plot comparison (c) scavenger experiment on D1/10V catalyst (d) catalytic recyclability for D1/10V catalyst.

both Cd-doped Ag_2O (D1) and $BiVO_4$ (V0) parts of the composite got photo-excited. The photoexcited electrons of the D1 component quenched the photoexcited VB holes in $BiVO_4$. Such a Z-scheme electron transfer mechanism causes the accumulation of photoexcited holes in the D1's VB and electrons in the $BiVO_4$ CB. CIP molecules got oxidized on the holes in the VB of D1. DFT calculations and MeCN control experiment results indirectly indicate that H_2O molecules also oxidize on D1's VB, producing oxygen (O_2). The photoexcited electrons in the $BiVO_4$ CB further reduce the O_2 molecules to form superoxide ($O_2^{-\bullet}$) radicals. The $O_2^{-\bullet}$ also degrade CIP.[36] The scavenging experiment results support this photocatalytic mechanism involving the main reactive species, *i.e.*, h^+ and O_2^-.

When D1 was the photocatalyst, then CIP got degraded only *via* VB oxidation. Note that, there was no production of superoxide radical ($E^0_{O_2/O_2^{-\bullet}} = -0.3$ V) (ref. 37) due to the inadequate CB position (1.2 eV) of D1. Therefore, the simultaneously generated CB electrons on the D1 caused its photo-corrosion. In contrast, the composite photocatalyst operates through a Z-scheme electrons transfer mechanism between the component parts (D1 and V0). CIP and H_2O got oxidized on the VB of the D1 component. At the same time, superoxide radicals are produced on the CB of the V0 ($BiVO_4$) by the reduction of O_2. Thus, these two redox reactions occur simultaneously on the heterostructure. Consequently, the recyclability of D1/10V is significantly better than that of the D1 photocatalyst.

Table 2 Comparison of photocatalytic CIP degradation turnover frequencies (TOF) of different composites

Photocatalysts	TOF (mol g^{-1} min^{-1})	Light source	Reference
BiOCl/Cu doped Bi_2S_3	4.42×10^{-6}	300 W Xe lamp	31
g-C_3N_4/Ti_3C_2	1.81×10^{-6}	500 W Xe lamp	32
Bi_2WO_6/Ta_3N_5	7.35×10^{-7}	300 W Xe lamp	33
Fe_2O_3/Bi_2WO_6	2.21×10^{-7}	300 W Xe lamp	34
Cd doped Ag_2O/$BiVO_4$	2.97×10^{-6}	14 W LED lamp	**This work (D1/10V)**

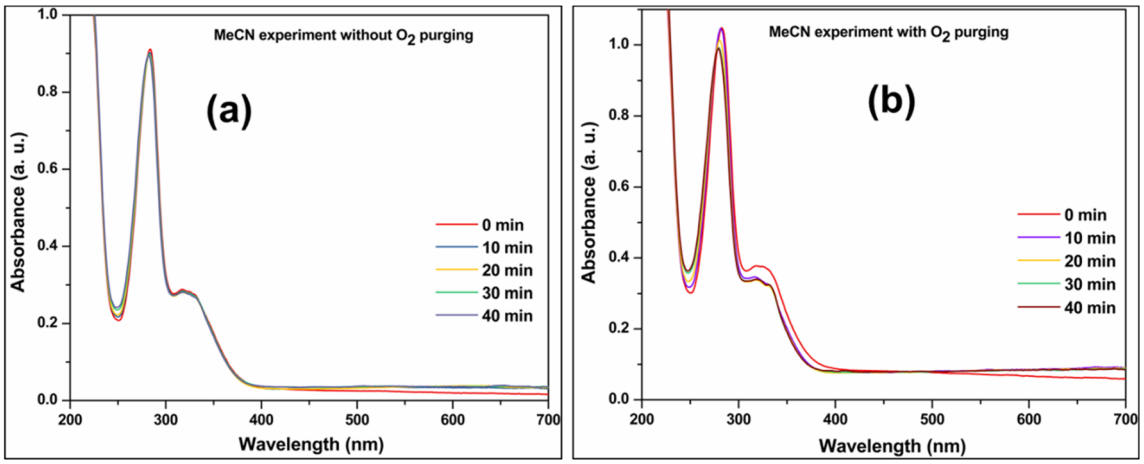

Fig. 7 UV-visible absorbance spectra of CIP degradation on D1/10V photocatalyst (a) MeCN solvent (b) MeCN solvent and O_2 purging.

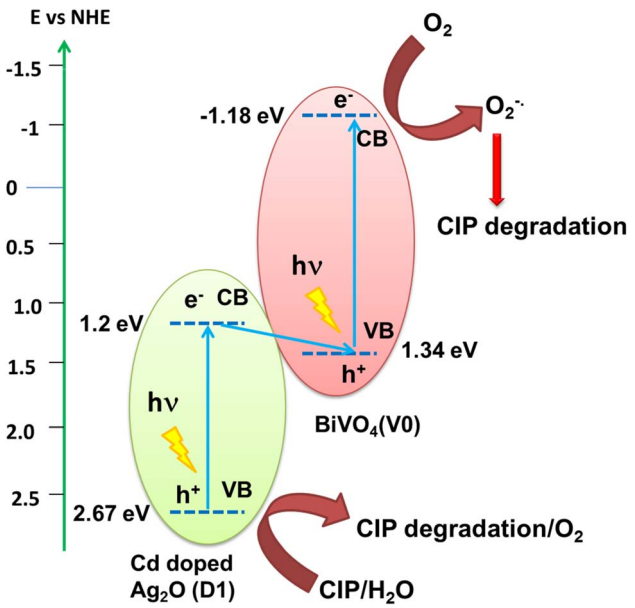

Fig. 8 A schematic of the proposed mechanism based on the experimental and DFT calculation results.

4. Conclusions

Cd-doping of Ag_2O shifted the VB position drastically relative to Ag_2O. Such doping had little effect on the bandgap of the material. DFT formation energy calculations showed that Cd substituted Ag in the Ag_2O lattice. The XRD evidence also supported this result. The Cd-doped Ag_2O nanoparticles were effective photocatalysts for CIP degradation but with extremely poor recyclability. The second part of the investigation coupled $BiVO_4$ with Cd-doped Ag_2O nanostructures. These composites were efficient Z-scheme photocatalysts for CIP and also exhibited appropriate recyclability. DFT calculations demonstrated H_2O activation on Cd-doped Ag_2O. The XPS results indicate that the appreciably more positive VB of the Cd-doped Ag_2O can oxidize water molecules to produce oxygen. The latter is reduced by photoexcited electrons accumulated on $BiVO_4$ to superoxide radicals. DFT calculations support this result. The scavenging experiment results (and the MeCN control experiments) indicate CIP oxidation on photoexcited VB holes in the (Cd-doped Ag_2O/$BiVO_4$) composite. Such a self-sustaining photocatalytic cycle increases the recyclability of composite significantly. Thus, doping of small bandgap semiconductors can change their electronic structure appreciably. Moreover, their composite with another visible range bandgap semiconductor can be used to design a new photocatalyst.

Conflicts of interest

There are no conflicts to declare.

Acknowledgements

Arup Kumar De acknowledges financial support received from IIT (BHU) and Central Instrument Facility (CIF) for providing the characterizing facilities. The authors also acknowledge CCIS (the Institute's computational facilities) for all the computational analysis.

References

1 J. Liu, D. Wang, K. Huang, J. Dong, J. Liao, S. Dai, X. Tang, M. Yan, H. Gong, J. Liu, Z. Gong, R. Liu, C. Cui, G. Ye, X. Zou and H. Fei, *ACS Nano*, 2021, **15**, 18125–18134.
2 Y. Gong, Z. Yang, L. Lari, I. Azaceta, V. K. Lazarov, J. Zhang, X. Xu, Q. Cheng and K. H. L. Zhang, *ACS Appl. Mater. Interfaces*, 2020, **12**, 53446–53453.
3 Y. Negishi, K. Munakata, W. Ohgake and K. Nobusada, *J. Phys. Chem. Lett.*, 2012, **3**, 2209–2214.
4 G. Murali, J. K. R. Modigunta, S. Park, S. Lee, H. Lee, J. Yeon, H. Kim, Y. H. Park, S. Y. Park, J. R. Durrant, H. Cha, T. K. An and I. In, *ACS Appl. Mater. Interfaces*, 2021, **13**, 34648–34657.
5 H. Li, Y. Xia, Z. Liang, G. Ba and W. Hou, *ACS Appl. Energy Mater.*, 2020, **3**, 377–386.

6 G. Natu, P. Hasin, Z. Huang, Z. Ji, M. He and Y. Wu, *ACS Appl. Mater. Interfaces*, 2012, **4**, 5922–5929.
7 J. Wang, T. Fang, L. Zhang, J. Feng, Z. Li and Z. Zou, *J. Catal.*, 2014, **309**, 291–299.
8 J. Chen, Y. Xiong, M. Duan, X. Li, J. Li, S. Fang, S. Qin and R. Zhang, *Langmuir*, 2020, **36**, 520–533.
9 S. Panneri, P. Ganguly, M. Mohan, B. N. Nair, A. A. P. Mohamed, K. G. Warrier and U. S. Hareesh, *ACS Sustainable Chem. Eng.*, 2017, **5**, 1610–1618.
10 I. Andjelkovic, D. Stankovic, J. Nesic, J. Krstic, P. Vulic, D. Manojlovic and G. Roglic, *Ind. Eng. Chem. Res.*, 2014, **53**, 10841–10848.
11 H. Xu, J. Xie, W. Jia, G. Wu and Y. Cao, *J. Colloid Interface Sci.*, 2018, **516**, 511–521.
12 A. K. De, S. Majumdar, S. Pal, S. Kumar and I. Sinha, *J. Alloys Compd.*, 2020, **832**, 154127.
13 F. A. Kiani, U. Shamraiz and A. Badshah, *Mater. Res. Express*, 2019, **7**, 015035.
14 A. K. De and I. Sinha, *J. Phys. Chem. Solids*, 2022, **167**, 110733.
15 G. Liu, J. Xu, T. Chen and K. Wang, *Phys. Rep.*, 2022, **981**, 1–50.
16 G. Liu, K. Du, S. Haussener and K. Wang, *ChemSusChem*, 2016, **9**, 1–28.
17 R. Su, M. He, N. Li, D. Ma, W. Zhou, B. Gao, Q. Yue and Q. Li, *SSRN Electron. J.*, 2022, **14**, 31920–31932.
18 M. Z. Shahid, R. Mehmood, M. Athar, J. Hussain, Y. Wei and A. Khaliq, *ACS Appl. Nano Mater.*, 2021, **4**, 746–758.
19 J. Chen, T. Tang, W. Feng, X. Liu, Z. Yin, X. Zhang, J. Chen and S. Cao, *ACS Appl. Nano Mater.*, 2022, **5**, 1296–1307.
20 Z. Xu, Y. Gu, Y. An, C. Zhang, Y. Yu, A. Long and L. Huang, *ACS Appl. Nano Mater.*, 2022, **5**, 931–938.
21 A. Mirzaei, A. Seck, D. Ma and M. Chaker, *ACS Appl. Nano Mater.*, 2022, **5**, 7161–7174.
22 P. Sahu and D. Das, *Langmuir*, 2022, **38**, 4503–4520.
23 L. Chen, H. Hua, Q. Yang, J. Liu, X. Han, Y. Li, C. Zhang, X. Wang and C. Hu, *J. Phys. Chem. C*, 2019, **123**, 1817–1827.
24 S. Ullah, Fayeza, A. A. Khan, A. Jan, S. Q. Aain, E. P. F. Neto, Y. E. Serge-Correales, R. Parveen, H. Wender, U. P. Rodrigues-Filho and S. J. L. Ribeiro, *Colloids Surf., A*, 2020, **600**, 124946.
25 L. Zhu, B. Wei, L. Xu, Z. Lü, H. Zhang, H. Gao and J. Che, *CrystEngComm*, 2012, **14**, 5705–5709.
26 R. Davis, A. Markham and J. A. Balfour, *Drugs*, 1996, **51**, 1019–1074.
27 D. Sharma, R. P. Patel, S. T. R. Zaidi, M. M. R. Sarker, Q. Y. Lean and L. C. Ming, *Front. Pharmacol.*, 2017, **8**, 546.
28 U. Kumar, J. Kuntail, A. Kumar, R. Prakash, M. R. Pai and I. Sinha, *Appl. Surf. Sci.*, 2022, **589**, 153013.
29 Z. Lu, Z. Yu, J. Dong, M. Song, Y. Liu, X. Liu, Z. Ma, H. Su, Y. Yan and P. Huo, *Chem. Eng. J.*, 2018, **337**, 228–241.
30 N. Jatav, J. Kuntail, D. Khan, A. Kumar De and I. Sinha, *J. Colloid Interface Sci.*, 2021, **599**, 717–729.
31 F. Du, Z. Lai, H. Tang, H. Wang and C. Zhao, *Chemosphere*, 2022, **287**, 132391.
32 N. Liu, N. Lu, Y. Su, P. Wang and X. Quan, *Sep. Purif. Technol.*, 2019, **211**, 782–789.
33 S. Li, J. Chen, S. Hu, H. Wang, W. Jiang and X. Chen, *Chem. Eng. J.*, 2020, **402**, 126165.
34 S. Y. Song, H. D. Chen, C. X. Li, D. S. Shi, Y. Ying, Y. B. Han, J. C. Xu, B. Hong, H. X. Jin, D. F. Jin, X. L. Peng, H. L. Ge and X. Q. Wang, *Chem. Phys.*, 2020, **530**, 110614.
35 Y. Kofuji, Y. Isobe, Y. Shiraishi, H. Sakamoto, S. Ichikawa, S. Tanaka and T. Hirai, *ChemCatChem*, 2018, **10**, 2070–2077.
36 H. Zhang, W. Wu, Y. Li, Y. Wang, C. Zhang, W. Zhang, L. Wang and L. Niu, *Appl. Surf. Sci.*, 2019, **465**, 450–458.
37 W. H. Koppenol, D. M. Stanbury and P. L. Bounds, *Free Radical Biol. Med.*, 2010, **49**, 317–322.